JMEPEG (2018) 27:2263–2270
https://doi.org/10.1007/s11665-018-3159-3

Phase Transformation and Lattice Parameter Changes of Non-trivalent Rare Earth-Doped YSZ as a Function of Temperature

Shengli Jiang, Xiao Huang, Zhang He, and Andrew Buyers

(Submitted April 30, 2017; in revised form August 27, 2017; published online January 23, 2018)

To examine the effect of doping/co-doping on high-temperature phase compositions of YSZ, stand-alone YSZ and CeO_2 and Nb_2O_5 co-doped YSZ samples were prepared using mechanical alloy and high-temperature sintering. XRD analysis was performed on these samples from room temperature to 1100 °C. The results show that the structure for the co-doped samples tends to be thermally stable when the test temperature is higher than a critical value. Monoclinic phase was dominant in Nb_2O_5 co-doped YSZ at temperatures lower than 600 °C, while for the YSZ and CeO_2 co-doped YSZ, cubic/tetragonal phase was dominant in the whole test temperature range. The lattice parameters for all the samples increase with increasing test temperature generally. The lattice parameters for the two non-trivalent rare earth oxides co-doped YSZ show that the lattice parameter a for the cubic phase of the Ce^{4+} co-doped YSZ is consistently greater than that of 7YSZ which is related to the presence of larger radius of Ce^{4+} in the matrix. The lattice parameters a, b, c for the monoclinic phase of Ce^{4+} co-doped YSZ are much closer to each other than that of the Nb^{5+} co-doped YSZ, indicating the former has better tendency to form cubic/tetragonal phase, which is desired for vast engineering applications.

Keywords CeO_2, co-doped, Nb_2O_5, XRD analysis, YSZ

1. Introduction

The demand for increasing gas turbine efficiency and higher firing temperature has pushed the superalloys to their upper limits of temperature capability and thermal stability. To lower the surface temperatures of gas turbine components, made of superalloys, and to prevent failure of components due to incipient melting, creep, oxidation, thermal fatigue and other modes of degradation, the application of thermal barrier coatings (TBCs) to the combustor and high-pressure turbine blades and vanes has become a necessity for modern gas turbines, in addition to complex internal cooling schemes (Ref 1).

Development of TBC systems has been summarized in our work (Ref 2). Zirconia has three crystal forms according to temperature (Ref 3):

$$\text{Monoclinic} \underset{950\,^\circ\text{C}}{\overset{1180\,^\circ\text{C}}{\rightleftarrows}} \text{Tetragonal} \overset{2370\,^\circ\text{C}}{\rightleftarrows} \text{Cubic} \overset{2680\,^\circ\text{C}}{\rightleftarrows} \text{Liquid}$$

The 4% volume difference between monoclinic phase and tetragonal phase (Ref 4) will cause coating failure under thermal recycling situation. Stabilization of tetragonal phase is always a key issue in TBC development, in which addition of rare earth oxide has been very effective. Yttria-stabilized zirconia (YSZ) is widely used in aircraft engine although it needs further improvement. In a previous work (Ref 2), yttria-stabilized zirconia (YSZ) co-doped with trivalent oxide Sc_2O_3 and Yb_2O_3 bulk material is prepared using mechanical alloying and high-temperature sintering. It is different from experimental data on phase stability of TBCs based on plasma-sprayed or EB-PVD coatings where the uncertainty in porosity and anisotropic microstructure may influence the phase transformation process (Ref 5). To resolve this problem, attempts to find new deposition method were performed in recent years. For example, plasma-assisted chemical vapor deposition (Ref 6) allows to deposit homogeneous, well-adhesive coatings at lower temperature on different substrates, but it is not known whether it is suitable for YSZ system. Therefore, further study on mechanical alloying and high-temperature sintering method for YSZ system is necessary.

In the literature (Ref 2), high-temperature XRD analysis was performed to study the phase transformation and lattice parameter changes of various phases in the baseline YSZ and co-doped samples. It was concluded that the structure for the co-doped samples tends to be more thermally stable at test temperature above critical value. The lattice parameters for all samples increase with temperature at which XRD is carried out, and the lattice parameters for the two trivalent rare earth oxides co-doped YSZ are smaller than that for 7% (mol) yttria-stabilized zirconia (7YSZ) under the same temperature. Recently, another work (Ref 7) also discussed phase stability of RE_2O_3 (RE = La, Nd, Gd, Yb) and Yb_2O_3 co-doped Y_2O_3-stabilized ZrO_2 ceramics and concluded that the phase stability of the compounds increased with the decrease in the RE^{3+} size,

---

Shengli Jiang, CAS Key Laboratory of Nuclear Materials and Safety Assessment, Institute of Metal Research, Chinese Academy of Sciences, Shenyang, People's Republic of China and Department of Mechanical and Aerospace Engineering, Carleton University, Ottawa, Canada; **Xiao Huang**, Department of Mechanical and Aerospace Engineering, Carleton University, Ottawa, Canada; and **Zhang He** and **Andrew Buyers**, Canadian Nuclear Laboratories, Chalk River, ON, Canada. Contact e-mail: sljiang@imr.ac.cn.

which could be attributed to the reduced driving force for t′ phase partitioning.

However, information on the effects of non-trivalent co-dopants, such as tetravalent dopants and pentavalent dopants, on the microstructure of the multiple component-doped zirconia bulk material is scarce. To understand how the phase composition of co-doped YSZ changes as a function of temperature, mechanically alloyed and sintered CeO_2 and Nb_2O_5 co-doped zirconia systems with yttria as primary stabilizer were investigated by high-temperature XRD in this study.

2. Experimental Procedures

2.1 Materials

Starting materials were high-purity crystalline 7YSZ obtained from Praxair Surface Technology. The powder specifications for 7YSZ are given in Table 1. Cerium oxide CeO_2 and niobium oxide Nb_2O_5 were selected as co-dopants. The dopant powder specifications are listed in Table 2.

These metal oxide powders were added to 7YSZ powder according to the targeted compositions of 7YSZ-3.945 mol.% Nb_2O_5 (3.9NbYSZ) and 7YSZ-5 mol.% CeO_2 (5CeYSZ), respectively. The reason for selecting 3.945 mol.% Nb_2O_5 was to completely annihilate the vacancies in the lattice structure of 7YSZ (with about 3.945 mol.% of trivalent Y_2O_3), while 5CeYSZ was based on reaching a total 12 mol.% of cation dopants in the ZrO_2 lattice structure. The final compositions of these metal oxide dopants and the associated concentrations of Y cation are shown in Table 3.

2.2 Bulk Sample Fabrication Approach

Sintering is used in this study to produce dense, crack-free and chemically homogeneous bulk ceramic materials. During sintering, the compacted bodies will generally experience three mechanisms of diffusion, i.e., surface diffusion at low temperature, resulting in neck growth between particles; grain boundary diffusion at elevated temperatures, capable of achieving relative densities of 90-95%; and lattice diffusion during the final stage, caused by the movement of point defects through the bulk of the lattice, controlling the grain growth and the chemical homogeneity of the final bulk material, which were mentioned in a previous study (Ref 2).

Table 1 Powder specifications for 7YSZ

Manufacturer	Praxair surface technology
Powder size, mesh	325
Composition	3.945 mol.% Y_2O_3—ZrO_2
Purity, %	99.9

Table 2 Powder specifications for co-dopants

Co-dopants	Powder specifications	
CeO_2	Manufacturer	Metall Rare Earth Limited
	Primary particle size, µm	1-10
	Purity, %	99.9
Nb_2O_5	Manufacturer	Sigma-Aldrich
	Primary particle size, µm	$<<1$
	Purity, %	99.9

Ceramic materials with ionic bond have very high activation energies for lattice diffusion (Ref 8); as such, to increase the rate of sintering, the sintering temperatures required are therefore very high. However, smaller particle size and narrow particle-size distributions will provide higher surface energy and reduced activation energies, thus increasing the sintering rate. Considering all the factors affecting the sintering behavior, the following process steps were developed and utilized in this study.

1. Powder blends were mixed and comminuted to mix powders and obtain finer powder size.
2. Powders were packed (with few drops of binder) into a mold by a hydraulic press to form high-density green bodies so that the diffusion distance would be shortened and mass transport rate increased.
3. Green bodies were heated to burn off the binder before sintering.
4. For ZrO_2 ceramic powders with particle sizes of 40-260 µm, the grain boundary diffusion and densification of the compact body occurred within the temperature range of 1100-1300 °C. The lattice diffusion and the $ZrO_2 + Y_2O_3$ reaction took place within the temperature range of 1300-1500 °C (Ref 9). So the sintering temperature was selected to be at 1500 °C which is the same as our previous study on trivalent rare earth-doped YSZ (Ref 2).The step-by-step procedure for the fabrication of bulk zirconia with metal oxide dopants is shown in Fig. 1 (Ref 2). Three samples were used for each situation.

2.3 Powder Blending and Comminuting

The powder blending was performed using a ball-milling method. To prevent contamination, pure ZrO_2 balls of 10 mm diameter were selected as a mixing medium. A neoprene barrel with quick-sealed, leakproof closures is 115 mm (4.5″) in diameter and 120 mm (4.75″) in height. In the experiment, the barrel was filled with 860 g (1.9 lb) zirconia balls and 454 g (1 lb) starting powders and placed on a Turbula T2C mix shaker (W. A. Bachofen AG Maschinenfabrik CH-4005 Basel/Schweiz). The rotation of the shaker was set to its lowest speed of 20 revolutions per minute (rpm) to avoid overheat inside the mill due to friction. The total blending time for all powders was 50 h with 1 h off every 2 h. Figure 2 shows the morphology of powders after ball milling for 20 and 50 h. As illustrated, the powders seem to be well mixed after 20 h. Extended mixing did not seem to vary the powder size noticeably.

2.4 Powder Compact

As mentioned in our previous work (Ref 2), the effect of compact pressure on green density and sintering density for micro-sized 8YSZ powders has been examined (Ref 9). The results indicated that increasing the compaction pressure beyond 150 MPa did not result in higher sintered density. Thus, in our experiment, a uniaxial pressure of 200 MPa was used. All powders were pressed with 25-mm-diameter cylindrical dies. To prevent cross-contamination, different dies were used for each specific composite powder. The dies were made from precipitation-hardened stainless steel (17-4PH), and the surfaces were well polished to reduce friction between the

Table 3 Compositions of the dopant cations in doped 7YSZ systems

Sample ID	Oxide, mol.%	Cation, mol.%	Final, mol.% of Y^{3+}
5CeYSZ	5 mol.% CeO_2	4.71 mol.% of Ce^{4+}	7.23
3.9NbYSZ	3.945 mol.% Nb_2O_5	7.05 mol.% of Nb^{5+}	7.06

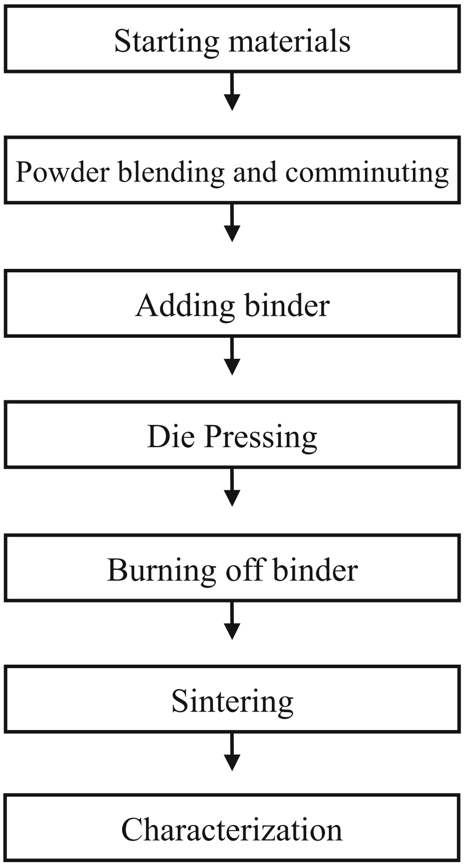

Fig. 1 Flowchart for the fabrication of bulk materials with doped metal oxides

particles and the wall. Before the milled powders were loaded into the die, a small amount of cellulose binder was added to strengthen the green body. After the pressure was applied for 10 min, the compacted body was ejected from the die. To facilitate sample removal, the cylindrical dies were sprayed with PTFE (Rocol) mold release spray.

2.5 Sintering Process

The samples were sintered in an air furnace (Lindberg/Blue BF51333C). The heating rate was 3.0-4.0 °C/min from room temperature to a soak temperature of 1500 °C. The soak time was 120 h. After sintering, the samples were furnace-cooled at a cooling rate between 4.6 and 1.5 °C/min.

2.6 High-Temperature X-ray Diffraction Analysis

The phases present in each sample after sintering were analyzed using x-ray diffraction (XRD) technique at room temperature, 100, 200, 300, 400, 500, 600, 700, 800, 900, 1000, and 1100 °C, respectively. The XRD measurements were performed on a Rigaku Ultima IV instrument using Kα copper radiation. The instrument is equipped with a hot stage and can reach a maximum temperature of 1200 °C. To minimize any peak position errors during the heating process, due to thermal expansion of components, the machine was configured in parallel beam geometry. The diffracted beam also had a flat monochromator paired with that geometry and a scintillation detector. The parameters chosen for the XRD analysis were the following: Full scan from 15° to 125° (2θ) was performed on each sample pre- and post-heating. Partial scan was used during the heating from 25° to 55° (2θ) with a step size (2θ) of 0.01° and counting time of 0.6 s/step.

To identify phases and estimate the proportion of each phase in the samples at room and elevated temperatures, a qualitative x-ray diffraction (XRD) technique was used. Lattice parameter a of cubic phase, a and c of tetragonal phase and a, b, c of monoclinic phase for the applicable samples were calculated to understand the changes in the lattice parameters, if any, with test temperature. All analyses of the XRD data (phase fraction and lattice parameters) were performed using MDI Jade 6 software (Ref 10).

3. Results and Discussion

3.1 SEM Observation

Figure 2 shows the morphology of powders after ball milling for different milling times. The maximum diameter of the powder was around 40 μm after ball milling for 20 h. It decreased to around 20 μm after ball milling for 50 h. The as-sintered samples were mounted and polished following standard metallographic procedure. The microstructures of sintered 7YSZ, 5CeYSZ, 3.9NbYSZ were examined using scanning electron microscope (SEM). As shown in Fig. 3, the three samples were well sintered with uniform grain structure and very little porosity. The grain size of 5CeYSZ was similar to that of 7YSZ, while the grain size of 3.9NbYSZ was obviously bigger.

3.2 XRD Analysis

The XRD patterns of all the samples studied are shown in Fig. 4. As presented in Fig. 4(a), the sintered 7YSZ contains all three phases (monoclinic m, tetragonal t and cubic c) at room temperature, although the t and c peaks are overlapped. The peak locations of monoclinic m, tetragonal t and cubic c can be confirmed in the literature (Ref 7, 11). Compared to 7YSZ, the monoclinic phase peaks (m) in 5CeYSZ (Fig. 4b) are much smaller and exist only between room temperature and temperatures up to 500 °C. This suggests the strong effect of co-dopant CeO_2 in stabilizing the $t + c$ phase to lower temperatures. For the Nb_2O_5 co-doped YSZ sample 3.9NbYSZ, the monoclinic phase is dominant at temperatures up to 500 °C, and there is still evidence of monoclinic phase peak at 600 °C

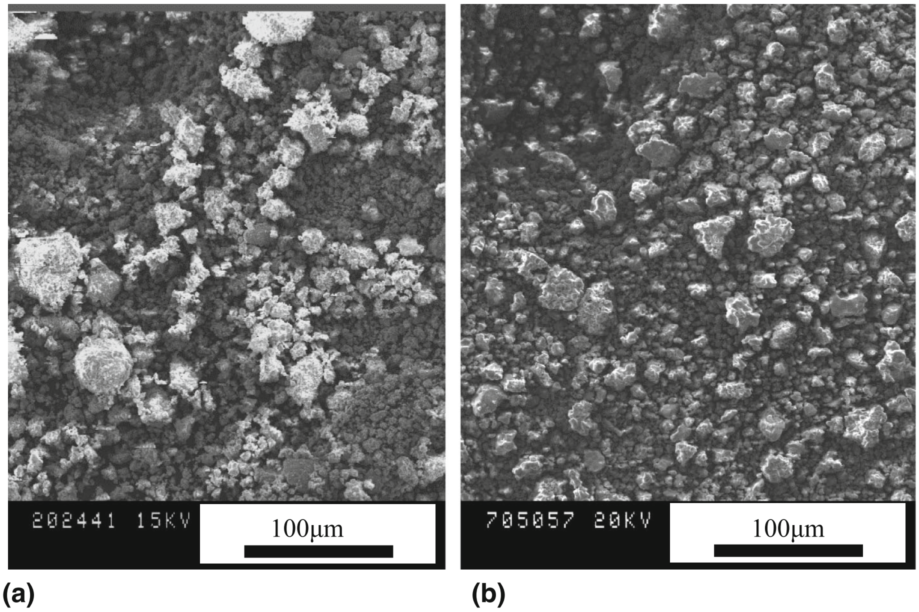

Fig. 2 SEM image of powders after ball milling for: (a) 20 h and (b) 50 h

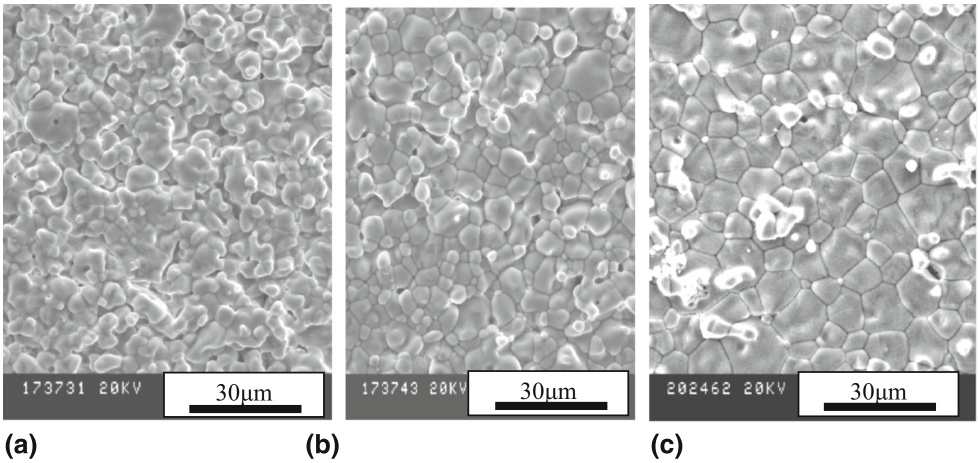

Fig. 3 SEM micrographs of sintered samples: (a) 7YSZ as-sintered surface, (b) 5CeYSZ as-sintered surface and (c) 3.9NbYSZ as-sintered surface

(Fig. 4c). This is due to the lack of oxygen vacancies in the sample when trivalent and pentavalent dopants are added in equal amount. When temperature is further increased above 700 °C, monoclinic peaks in all three samples can no longer be observed.

The quantitative measurements for the phase fractions are presented in Fig. 5, where both the mol.% of $c + t$ and m phase are plotted as a function of time. It is noted that the $m \rightarrow t$ transformation starts right after 500 °C for 3.9NbYSZ and the transformation is completed at 700 °C. At temperatures between 700 and 1100 °C, only t phase is present in sample 3.9NbYSZ. The $m \rightarrow t$ transformation starts at a higher temperature for 7YSZ, and it also finishes at around 700 °C. The same phase transformation $m \rightarrow t$ occurred in 5CeYSZ is more gradual and starts right after 300 °C.

The above-described phase transformation of $m \rightarrow t$ can be compared to the binary Y_2O_3-ZrO_2 phase diagram shown in Fig. 6 (Ref 12). Position A shows the cooling line of 7YSZ and 5CeYSZ (x-axis represents mol. % of oxygen vacancy), and position B shows that of 3.9NbYSZ. The ratios of both monoclinic to cubic + tetragonal phase (in 7YSZ and 5CeYSZ) and to tetragonal phase (in 3.9NbYSZ) decrease with temperature gradually, as shown in the phase diagram, as well as that reported in the published literature (Ref 13). However, based on the phase fractions versus temperature (Fig. 4), this reduction in monoclinic phase in 7YSZ and 5CeYSZ occurred more rapidly than that represented in the phase diagram. Furthermore, the transformation temperatures of $m \rightarrow t$ in 5CeYSZ and 3.9NbYSZ deviate from that shown in this binary diagram.

The stability of tetragonal or cubic ZrO_2 at room temperature could be altered by either increasing the lattice parameters or introducing oxygen vacancies to the crystal (Ref 14). Therefore, the existence of oxygen vacancies or larger substituting cations could play a role controlling phase transformations of zirconia polycrystals (Ref 15). When a metal oxide or dopant with a cation valence less than that of Zr atom is added

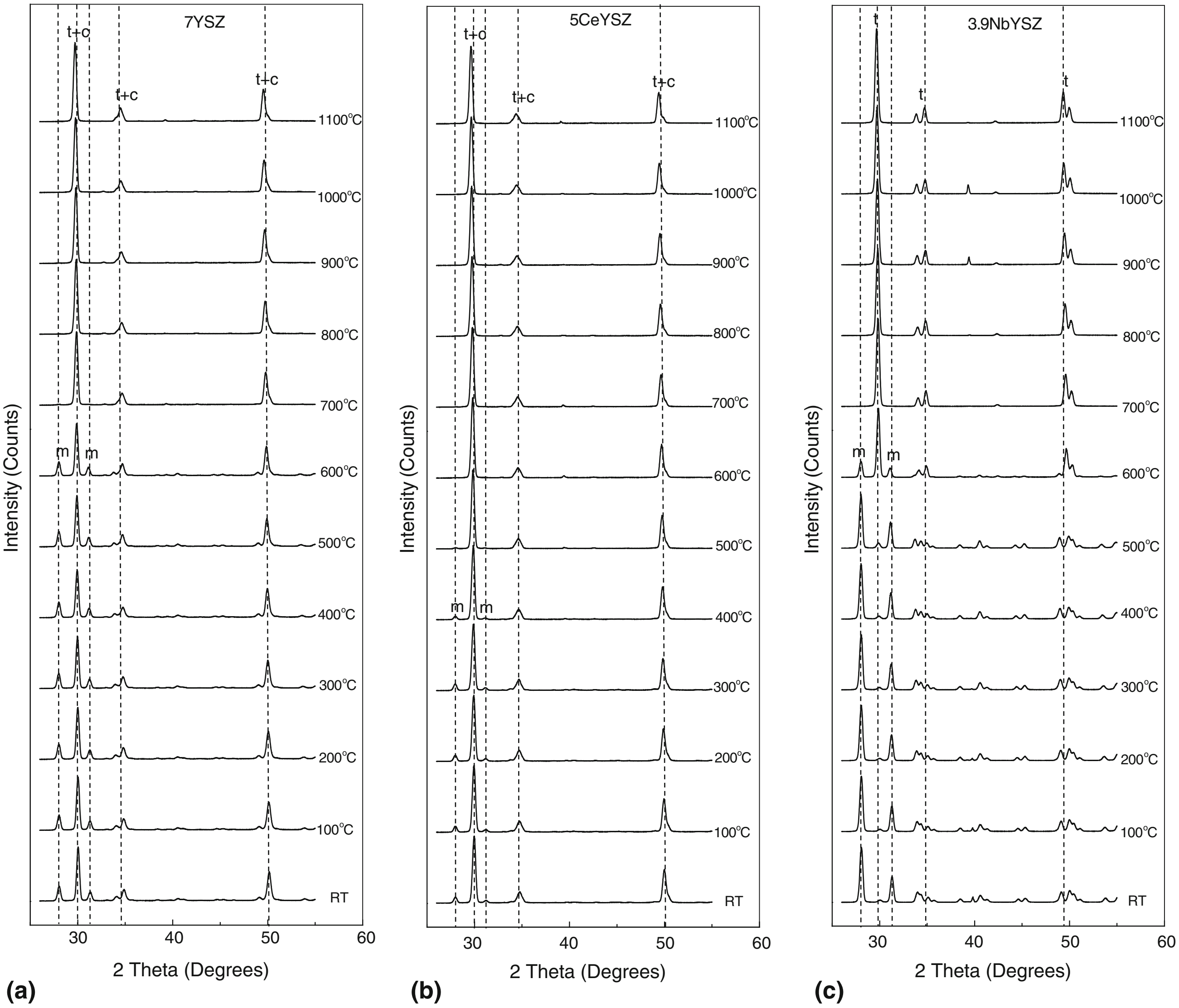

Fig. 4 XRD patterns of (a) 7YSZ, (b) 5CeYSZ and (c) 3.9NbYSZ

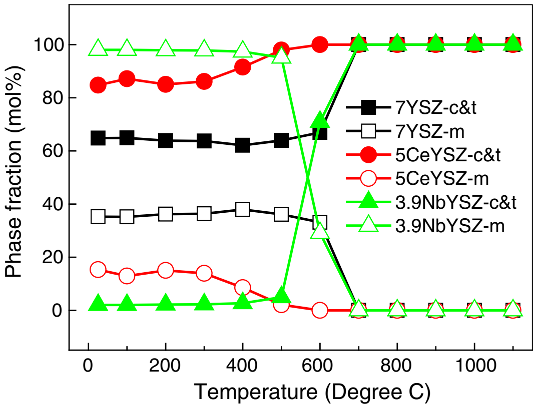

Fig. 5 Variation in phase fraction of the materials as a function of XRD test temperature

to zirconia, either cation interstitials or anion vacancies must form in order to maintain the charge balance. For doped zirconia, the preferred structure is that the cation Zr^{4+} is replaced by the cation of the dopant instead of forming cation interstitials since the reaction energy to form an oxygen vacancy is much lower than that for a cation interstitial (Ref 16). Bivalent and trivalent metal oxides, such as MgO, CaO, Y_2O_3, Yb_2O_3 and Sc_2O_3, have been proven to be effective stabilizers for $t + c$ phases (Ref 17) as oxygen vacancies stabilize the high-temperature phases. The coordination number of a zirconium atom in tetragonal and cubic phases is eight, while in the monoclinic phase it is seven. Zirconium atoms have a tendency for a coordination number lower than eight at room temperature, which makes the tetragonal or cubic phase unstable (Ref 14). The introduction of oxygen vacancies enables the zirconium cation to be surrounded by seven oxygen anions instead of eight while still maintaining the fluorite structures; this effectively stabilizes the high-temperature phases.

The CeO_2 co-doped 7YSZ is tetravalent; no additional oxygen vacancies could be generated to impart stabilization effect. However, the substitution of zirconium ions Zr^{4+}

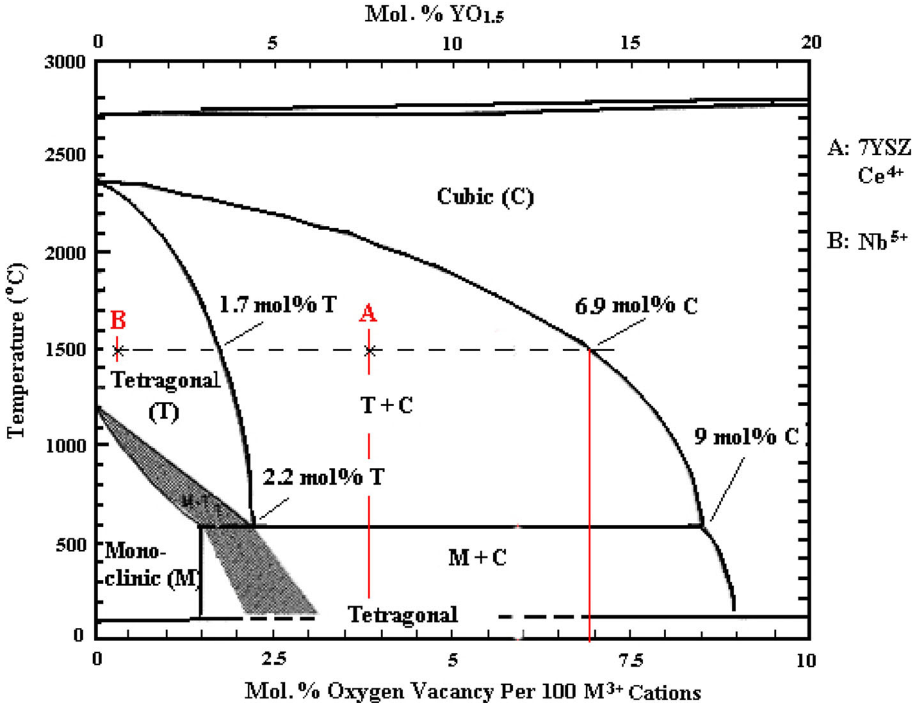

Fig. 6 Y2O3-ZrO2 binary phase diagram (Ref 9). Position A: 7YSZ, Ce^{4+}, position B: Nb^{5+}

Table 4 Calculated lattice parameter from the XRD patterns (10^{-1} nm or Å)

	7YSZ							5CeYSZ							3.9NbYSZ					
	Cubic	Monoclinic			Tetragonal			Cubic	Monoclinic			Tetragonal			Monoclinic			Tetragonal		
t, °C	*a*	*a*	*b*	*c*	*a*	*c*	*c/a*	*a*	*a*	*b*	*c*	*a*	*c*	*c/a*	*a*	*b*	*c*	*a*	*c*	*c/a*
25	5.135	5.312	5.210	5.164	…	…		5.154	5.126	5.112	5.108	…	…		5.326	5.203	5.165	…	…	
100	5.147	5.322	5.198	5.163	…	…		5.161	5.138	5.129	5.128	…	…		5.333	5.202	5.169	…	…	
200	5.149	5.326	5.198	5.167	…	…		5.170	5.128	5.128	5.124	…	…		5.339	5.203	5.174	…	…	
300	5.158	5.330	5.197	5.173	…	…		5.171	5.145	5.126	5.119	…	…		5.346	5.205	5.179	…	…	
400	5.163	5.333	5.194	5.179	…	…		5.178	5.137	5.128	5.126	…	…		5.355	5.207	5.186	…	…	
500	5.168	5.337	5.192	5.186	…	…		5.181	…	…	…	5.159	5.206	1.0092	5.365	5.208	5.192	5.100	5.185	1.0165
600	5.172	5.344	5.194	5.192	…	…		5.188	…	…	…	5.165	5.213	1.0094	5.336	5.222	5.204	5.120	5.237	1.0228
700	5.178	…	…		5.155	5.203	1.0093	5.192	…	…	…	5.171	5.219	1.0093	…	…	…	5.126	5.249	1.0239
800	5.182	…	…		5.158	5.206	1.0093	5.201	…	…	…	5.176	5.224	1.0093	…	…	…	5.132	5.257	1.0244
900	5.188	…	…		5.167	5.214	1.0091	5.206	…	…	…	5.181	5.229	1.0094	…	…	…	5.138	5.265	1.0248
1000	5.195	…	…		5.172	5.220	1.0092	5.213	…	…	…	5.188	5.235	1.0091	…	…	…	5.143	5.273	1.0252
1100	5.204	…	…		5.179	5.226	1.0090	5.218	…	…	…	5.196	5.243	1.0090	…	…	…	5.148	5.278	1.0252

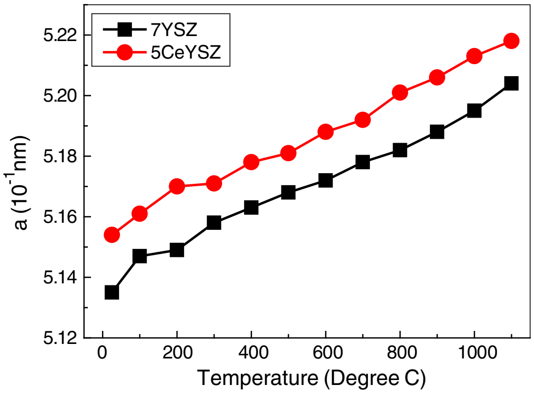

Fig. 7 Calculated lattice parameter of the cubic phase as a function of temperature

(0.072 nm) with larger cations such as Ce^{4+} (0.092 nm) will increase the lattice parameters, which in turn enables the eight coordination of oxygen anion to be stable at room temperature. This is clearly seen in this study where 7YSZ has close to 40% of *t* phase, while 5CeYSZ has less than 20% at room temperature (Fig. 5). Also the *m* → *t* transformation takes place at 400 °C in 5CeYSZ, 200 °C lower than that for 7YSZ.

The addition of Nb_2O_5 cancels out the vacancies existed in 7YSZ and plays a role of destabilizing *t* + *c* phases. In fact, monoclinic phase is a dominant phase in 3.9NbYSZ at low temperature (Fig. 4). In terms of cation size effect, Nb^{5+} has a radius of 0.069 nm, smaller than that of Zr^{4+}; thus, it does not contribute to the stabilization of *t* or *c* phase at low temperatures.

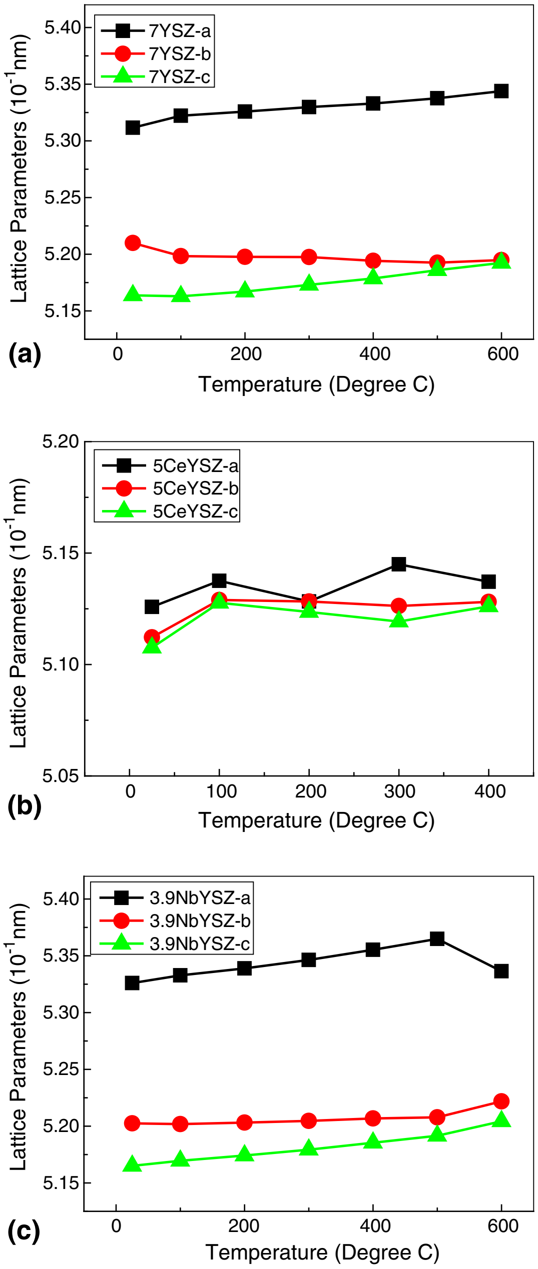

Fig. 8 Calculated lattice parameter of monoclinic phase as a function of temperature

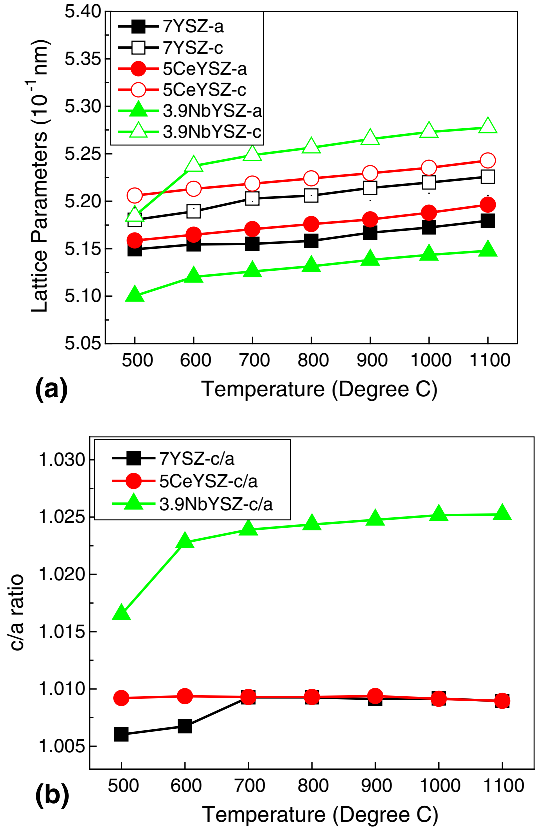

Fig. 9 Calculated lattice parameter of tetragonal phase as a function of temperature. (a) Lattice parameters a and c as a function of temperature, (b) *c/a* ratio

The XRD patterns recorded for each sample at different temperatures were analyzed using MDI Jade 6 software (Ref 10), and the lattice parameters for the each phase were calculated as a function of temperature (Table 4). The variation of lattice parameters *a* (10^{-1} nm) for the cubic phase (assuming cubic phase was dominant when peaks from both *c* and *t* were overlapped) as a function of temperature is shown in Fig. 7. (No *c* phase was observed in the 3.9NbYSZ within the test temperature range used in this study.) It can be seen that the lattice parameter for the c phase increases with test temperature for both 5CeYSZ and 7YSZ. This is in accordance with a previous work for cerium-doped zirconates (Ref 18). Furthermore, lattice parameter *a* of the main phase (cubic) for the Ce^{4+} co-doped YSZ is consistently greater when being compared to 7YSZ at the same temperature (Table 4). This is related to the larger radius of Ce^{4+}.

All the three samples contain *m* phase at temperatures lower than 600 °C. The variations in lattice parameters *a*, *b* and *c* for the monoclinic phase as a function of temperature are shown in Fig. 8. It can be seen that the lattice parameter *a* increases consistently with test temperature for 7YSZ (Fig. 8a) and 3.9NbYSZ (Fig. 8c), while the lattice parameters *b* and *c* tended to be closer to each other. Furthermore, for 7YSZ, as temperature increases from room temperature to 600 °C, the parameters *b* and *c* gradually converge, as *m* phase starts its transformation to *t* phase. For 3.9NbYSZ, the values of *b* and *c* also increase with temperature and converge to a lesser extent prior to the transformation. For 5CeYSZ, the values of all the three lattice parameters of monoclinic phase, *a*, *b* and *c*, are very similar and all are lower than that in 7YSZ and 3.9NbYSZ (Fig. 8b).

For the sintered samples tested at temperatures higher than 700 °C, tetragonal phase is present, from either *m* → *t* transformation or during cooling from sintering. The variation of lattice parameters *a* and *c* for the tetragonal phase as a function of temperature is shown in Fig. 9(a). As shown, the lattice parameters *a* and *c* increase with test temperature for all the three materials. Figure 9(b) presents the tetragonality, *c/a,* of the samples at different test temperatures. The *c/a* ratios for 7YSZ and 5CeYSZ are very similar; however, for 3.9NbYSZ, the *c/a* ratio is distinctly larger than that of 7YSZ and 5CeYSZ.

4. Conclusion

YSZ co-doped with CeO_2 and Nb_2O_5 rare earth oxides was prepared using mechanical alloying and high-temperature sintering. The produced samples were analyzed with high-temperature XRD to study the process of the associated phase transformation and the variation in lattice parameters as a function of temperature. It was observed that the co-dopant CeO_2 stabilized the cubic and tetragonal phase due to the addition of larger radius Ce^{4+} cations. The co-doping of Nb_2O_5 was disadvantageous in stabilizing the cubic or tetragonal phase due to its higher valency ($> +4$) and the smaller cation radius than that of Zr^{4+}. The addition of CeO_2 to YSZ reduced the amount of monoclinic phase formed during cooling from sintering temperature, suggesting its stabilizing ability in *t* and *c* phases, while the monoclinic phase became dominant after cooling for the Nb_2O_5 co-doped YSZ. The lattice parameters for all the samples increase with increasing XRD test temperature. The lattice parameters *b* and *c* of the monoclinic phase converged with temperature increase, indicating the transformation tendency from the monoclinic phase to the tetragonal phase.

References

1. A. Mensch and K.A. Thole, Overall Effectiveness of a Blade Endwall With Jet Impingement and Film Cooling, *J. Eng. Gas Turbines Power-Trans ASME*, 2014, **136**(3), p 031901
2. S.L. Jiang, X. Huang, and Z. He, Phase Transformation and Lattice Parameter Changes of Trivalent Rare Earth Doped YSZ as a Function of Temperature, *J. Mater. Eng. Perform.*, 2016, **25**(11), p 4686–4694
3. A.H. Heuer (ed) Review: Phase Transformations and Microstructural Characterization of Alloys in the System Y2O3-ZrO2, in Advances in Ceramics. ed. a.H.Y. N.Y. S Somiya, WesterviUe. 1988. P. 3–20
4. T.K. Gupta, J.H. Bechtold, and R.C. Kuznicki, Stabilization of Tetragonal Phase in Polycrystalline Zirconia, *Journal of Material Science*, 1977, **12**, p 2421
5. V. Kumar and B. Kandasubramanian, Processing and Design Methodologies for Advanced and Novel Thermal Barrier Coatings for Engineering Applications, *Particuology*, 2016, **27**, p 1–28
6. M. Janus et al., Plasma Assisted Chemical Vapour Deposition—Technological Design of Functional Coatings, *Arch. Metall. Mater.*, 2015, **60**(2), p 909–914
7. L. Guo, M. Li, and F. Ye, Phase Stability and Thermal Conductivity of RE2O3 (RE = La, Nd, Gd, Yb) and Yb2O3 Co-doped Y2O3 Stabilized ZrO2 Ceramics, *Ceram. Int.*, 2016, **42**(6), p 7360–7365
8. H. Siethoff, A single Law for the Activation Energies of Self-diffusion of Various Cubic Metals, Intermetallic Compounds, Ionic Crystals and Oxides, *Phys. Status Solidi B-Basic Solid State Phys.*, 2007, **244**(4), p 1296–1303
9. I.R. Gibson, G.P. Dransfield, and J.T.S. Irvine, Sinterability of Commercial 8 mol% Yttria-Stabilized Zirconia Powders and the Effect of Sintered Density on the Ionic Conductivity, *J. Mater. Sci.*, 1998, **33**(17), p 4297–4305
10. Material Data Inc, *MDI Jade 6 User's Manual*. 2004
11. D. Gosset and M. Le Saux, In-Situ X-ray Diffraction Analysis of Zirconia Layer Formed on Zirconium Alloys Oxidized at High Temperature, *J. Nucl. Mater.*, 2015, **458**, p 245–252
12. H.G. Scott, Phase Relationship in Zirconia-Yttria System, *J. Mater. Sci.*, 1975, **10**(9), p 1527–1535
13. W. Wang, S.Q. Qian, and H. Shen, Microstructure and Mechanical Properties of Yttria-Stabilized Zirconia Coatings Produced by Eletrophoretic Deposition and Microwave Sintering, *Metall. Mater. Trans. A-Phys. Metall. Mater. Sci.*, 2011, **42A**(11), p 3265–3268
14. A. Kuwabara et al., Influence of Interaction Between Neighboring Oxygen Ions on Phase Stability in Cubic Zirconia, *J. Am. Ceram. Soc.*, 2002, **85**(10), p 2557–2561
15. P. Kountouros and G. Petzow, Defect chemistry, phase stability and properties of zirconia polycrystals, *Science and Technology of Zirconia*, V.S. Badwal, M. Bannister, and R. Hannink, Ed., Technomic, Lancaster, Basel, 1993, p 30–48
16. A. Dwivedi and A.N. Cormack, A Computer-Simulation Study of the Defect Structure of Calcia-Stabilized Zirconia, *Philos. Mag. A-Phys. Condens. Matter Struct. Defects Mech. Prop.*, 1990, **61**(1), p 1–22
17. V.I. Aleksandrov et al., Synthesis and crystal growth of refractory materials by RF melting in a cold container, *Current Topics in Materials Science*, North-Holland Pub. Co.; Elsevier North-Holland, Amsetrdam, 1978, p 4210–4480
18. J.H. Zhang et al., Thermal Expansion and Solubility Limits of Cerium-Doped Lanthanum Zirconates, *J. Alloy. Compds*, 2012, **525**, p 78–81